

Experimental and numerical investigations of film flow behaviors in resonance section over corrugated plates

Ya-qiong GUO, Ning-xin LIU, Lai CAI, Wei-rong HONG^{†‡}

Institute of Process Equipment, College of Energy Engineering, Zhejiang University, Hangzhou 310027, China

[†]E-mail: hongwr@zju.edu.cn

Received Mar. 20, 2018; Revision accepted Aug. 31, 2018; Crosschecked Dec. 6, 2018

Abstract: The oscillation of gas–liquid interface is enhanced when film flows over a specific corrugation under certain flow conditions. The resonance phenomenon occurs when the free surface amplitude reaches its maximum. In this study, the resonance section is proposed for the first time in which the oscillation of the film surface is enhanced and bottom eddies are suppressed. The trend of the bottom eddies inspires the discovery of the resonance section. The dynamic characteristics of the resonance phenomenon were analyzed by simulations and experiments. The numerical simulations were performed with the open source software OpenFOAM, and the experiments were conducted by the particle image velocimetry (PIV) method. In the resonance section, the dynamic characteristics are different from the other sections: the upper and lower bounds of the resonance section correspond to the two inflection points of free surface amplitude, the variations in average liquid film thickness are slight, and the normal velocity intensity of the free surface is increased. Additionally, the enhancement of velocity intensity occurs within a region.

Key words: Film flow; Resonance section; OpenFOAM; Particle image velocimetry (PIV); Corrugated plate
<https://doi.org/10.1631/jzus.A1800191>

CLC number: TQ021.1; TQ053.5


1 Introduction

Film flow is a thin flow over a corrugated plate and has broad applications in aerospace, thermal engineering, chemical engineering, light industry, energy, petroleum, and refrigeration (Ho et al., 2004; Pak, 2011). The structured packing column is widely used in chemical processing, but the entire tower flow modeling involves significant computational work. Therefore, some researchers (Gu, 2004; Xu, 2010; Pavlenko et al., 2017) have simplified structural packing to an inclined corrugated plate. Li et al. (2015) found that the mass transfer efficiency of film flow over an irregular shape is three to five times higher

than over a flat one. Wu et al. (2016) verified this conclusion by numerical simulations. The heat (Nabil and Rattner, 2017; Wang et al., 2017) and mass transfer (Conn et al., 2017) characteristics of film flow are the focal research points of recent studies.

Resonance produces the largest free-surface area, which improves the mass transfer efficiency. Some researchers have studied film flow resonance by experiments, computational fluid dynamics (CFD) simulations, and theoretical methods. Bontozoglou and Papapolymerou (1997) discovered the surface resonance phenomenon of film flow over an inclined corrugated structure for the first time. They observed that surface amplitude increases to the maximum with increasing Reynolds numbers. The conclusion was verified by the finite element calculation (Malamaris and Bontozoglou, 1999) of the Navier–Stokes equation. Bontozoglou (2000) investigated higher harmonics and surface variations in different Reynolds numbers. He compared it with a film flow over a

[‡] Corresponding author

 ORCID: Ya-qiong GUO, <https://orcid.org/0000-0001-6196-7176>;
Wei-rong HONG, <https://orcid.org/0000-0002-8979-0488>

© Zhejiang University and Springer-Verlag GmbH Germany, part of Springer Nature 2019

flat plate, and found that the phase position varies with amplitude when the resonance phenomenon occurs. Argyriadi et al. (2006) studied the effect of wall steepness on film flow resonance by experiments. They concluded that the corrugation height has little effect on the resonance Reynolds number and free surface amplitude. Wierschem et al. (2008) and Heining et al. (2009) studied linear and nonlinear resonances of film flow over an inclined corrugated plate. They found the difference between linear and nonlinear analyses. Wierschem et al. (2010) and Schörner et al. (2016) discovered film flow resonance over a sinusoidal corrugated plate by numerical simulations and experiments. Wierschem et al. (2010) found that the resonance phenomenon suppresses eddies in the flow field. Schörner et al. (2016) found that resonance is attributed to the interplay between the topography's amplitude and inclination, as well as the fluid's viscosity. Tong et al. (2013) first discovered the resonance of film flow over a triangular corrugated plate by experiments. Through a theoretical study of falling film over an inclined corrugated plate, Trifonov (2014) obtained the relationship among the resonance Reynolds number, the inclined angle, and the Kapitza number. The subsequent research conducted by Trifonov (2016) revealed that the Reynolds number where resonance occurs depends on the period and amplitude of corrugation. Li (2015) discovered the resonance phenomenon of film flow over a trapezoidal corrugated plate for the first time.

Most of the studies on film flow resonance have emphasized the occurrence conditions, such as the shapes and steepness of corrugations. Investigations of resonance have been performed primarily on sinusoidal and triangular corrugations. However, the mechanism and how the resonance phenomenon affects the flow have not been formulated into a systematic study. When the amplitude of the interface becomes the maximum, the corresponding Reynolds number is defined as the resonance point. In industrial production, a region is more meaningful than a point. To enlarge the fluctuation of the interface in chemical processing, the operation condition is easier to achieve in a range of Reynolds numbers rather than a specific Reynolds number. Therefore, we show for the first time, in this study, that resonance section

mechanisms anticipating the scales of eddies suppression exist. It is meaningful to investigate the fluid dynamic characteristics in the resonance section. In this paper, the film flow over rectangular corrugations is studied by numerical simulations and experiments. In the simulations, the volume of fluid (VOF) method is applied to track the free surface between gas and liquid. In the experiments, the particle image velocimetry (PIV) method is conducted to calculate the velocity distribution.

2 Numerical model and experimental setup

2.1 Modeling

Paschke (2011) discovered that a complex corrugated structure is composed of a large number of tetrahedrons with opposite directions and staggered distributions. Therefore, the complex corrugation is simplified to be a 2D geometric plate. A corrugated plate consists of periodic rectangular corrugations and two flat plates for the transition. The flat plates are of the same length (0.1 m). Fig. 1 shows the structure of the rectangular corrugation. In this study, the height of the corrugation is $A=0.001$ m, and the wavelength of the corrugation is $L=0.01$ m. The total number of corrugations is 5, and the third corrugation is the primary study object. For the film flow over the periodically corrugated plate, when the period of wave is three or beyond, from the second period onward, the characteristics of film flow in each wave are very close. The inclined angle between the corrugated plate and the horizontal plane is 11° .

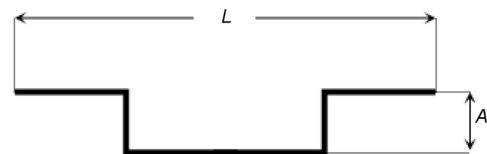


Fig. 1 Rectangular corrugation structure

A solver interFoam based on the VOF method in OpenFOAM is applied in the simulation. For the two-phase counterflow, the governing equations are as follows (Nieves-Remacha et al., 2015):

$$\nabla U = 0, \quad (1)$$

$$\begin{aligned} & \rho(\alpha) \left(\frac{\partial \mathbf{U}}{\partial t} + \nabla(\mathbf{U}\mathbf{U}) \right) \\ & = -\nabla p + \rho(\alpha) \mathbf{g} + \nabla \left[\rho(\alpha) (\nabla \mathbf{U} + (\nabla \mathbf{U})^T) \right] + f_{sv}. \end{aligned} \quad (2)$$

Eq. (1) is the continuity equation; Eq. (2) is the momentum equation. $\mathbf{U}=(u, v)$ is the velocity field, u is the tangential velocity, v is the normal velocity, t is the time, and p is the pressure. $\mathbf{g}=(g_0 \sin \beta, -g_0 \cos \beta)$, g_0 is the gravity acceleration, and β is the inclined angle between the corrugated structure and the horizon. ρ is the density. α is the phase factor and is defined as follows: $\alpha=0$ when the unit is full of air; $\alpha=1$ when the unit is full of liquid; $0<\alpha<1$ when the unit is filled with both types of flow. f_{sv} is the surface tension term. Based on Brackbill et al. (1992)'s view of the continuum surface force (CSF) method, the surface tension is as follows (Li et al., 2018):

$$f_{sv} = \sigma \kappa \mathbf{n}, \quad (3)$$

where σ is surface tension. \mathbf{n} is the normal vector of the free surface and

$$\mathbf{n} = \nabla \alpha. \quad (4)$$

κ is the averaged curvature of the free surface and

$$\kappa = -\nabla \hat{\mathbf{n}} = -\frac{\nabla \mathbf{n}}{|\mathbf{n}|}, \quad (5)$$

where $\hat{\mathbf{n}}$ is the unit normal vector of the free surface.

Hirt and Nichols (1981) developed the VOF method that is an efficient method to simulate surface topography problems. It is a type of volume tracking that uses a fixed Euler mesh through α (volume fraction of fluid in a mesh unit) to track the flow change. The functions $\rho(\alpha)$ and $\mu(\alpha)$ refer to the density and viscosity, respectively, and they are defined as

$$\rho(\alpha) = \rho_{\text{liquid}}(\alpha) + \rho_{\text{air}}(1 - \alpha), \quad (6)$$

$$\mu(\alpha) = \mu_{\text{liquid}}(\alpha) + \mu_{\text{air}}(1 - \alpha), \quad (7)$$

where ρ_{liquid} and μ_{liquid} are the density and viscosity of the liquid, respectively; ρ_{air} and μ_{air} are the density and viscosity of air, respectively.

The transport equation is defined as

$$\frac{\partial \alpha}{\partial t} + \nabla(\alpha \mathbf{U}) + \nabla[\alpha(1 - \alpha) \mathbf{U}_r] = 0, \quad (8)$$

where $\mathbf{U}_r = \mathbf{U}_{\text{liquid}} - \mathbf{U}_{\text{air}}$ is the relative velocity between the two phases.

Fig. 2 shows the 2D numerical model of a rectangular corrugation. The upper part represents the air region ($\alpha=0$) and the lower part represents the liquid region ($\alpha=1$).

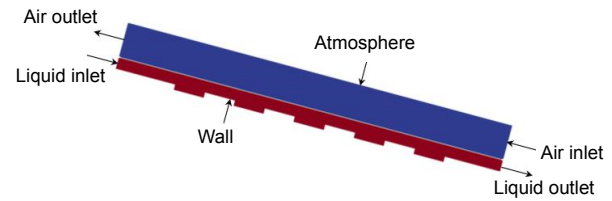


Fig. 2 The 2D numerical model

Reynolds number (Re) is a dimensionless parameter that represents the flow rate and can be defined as

$$Re = \frac{D_h \mathbf{U}_a}{\nu}, \quad (9)$$

where ν is the kinematic viscosity of the liquid. \mathbf{U}_a is the mean velocity of the liquid inlet. D_h is the hydraulic diameter and

$$D_h = \frac{4W\delta}{W + 2\delta}, \quad (10)$$

where W is the width of the channel, and δ is the thickness of liquid film at the inlet. Each grid would be a parallelogram structured grid (Appendix A). Gridding independence is validated in Appendix A. Table 1 shows the boundary conditions.

2.2 Experimental setup

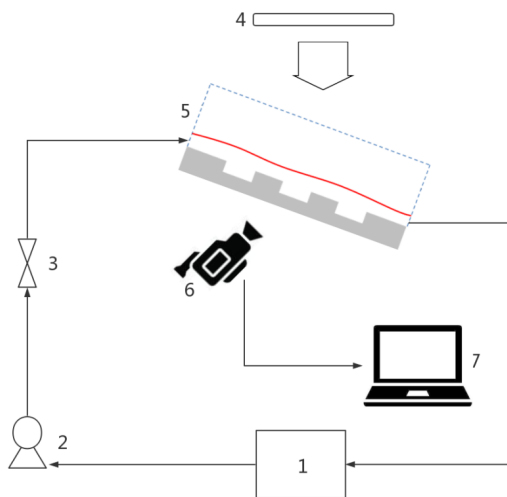
To obtain the indicators of the flow characteristics, the PIV method is used to measure the flow field. A large number of tracer particles are scattered in the liquid phase. A high-speed camera can record the positions of these particles at different instants of time. The velocities of different points are calculated by

Table 1 Boundary conditions

Item	Boundary condition		
	Velocity, u	Pressure, p	Phase fraction, α
Liquid inlet	Fixed value ($u_i, 0, 0$)	Zero gradient	Fixed value 1
Air inlet	Zero gradient	Zero gradient	Zero gradient
Liquid outlet	Zero gradient	Zero gradient	Zero gradient
Air outlet	Zero gradient	Zero gradient	Zero gradient
Wall	Fixed value ($0, 0, 0$)	Zero gradient	Constant alpha contact angle $\theta=90^\circ$
Atmosphere	Pressure inlet outlet velocity	Total pressure $p_0=0$	Zero gradient

image processing. The flow characteristics such as streamlines and liquid film thickness can be obtained.

Fig. 3 shows the experimental setup. The pump (2) pumps the liquid mixed with trace particles from the tank (1) into the channel (5). The valve (3) controls the flow rate of the liquid. The irradiation of continuous laser (4) illuminates the tracer particles in the flow field. The high-speed camera (6) records the positions of the particles. When the recording finishes, the data are passed to the computer (7) for image processing.

**Fig. 3** Sketch of the experimental setup

1: tank; 2: pump; 3: valve; 4: laser; 5: channel; 6: high-speed camera; 7: computer

3 Results and discussion

3.1 Flow fields analysis

Vlachogiannis and Bontozoglou (2002) defined the film flow resonance phenomenon. For a specific corrugated structure, the free surface amplitude

reaches the maximum at a particular Reynolds number. The free surface amplitude is the difference between the maximum and minimum of the free surface vertical ordinates in a corrugation period (Li et al., 2016).

Fig. 4 shows the flow fields over a rectangular plate. With an increase in Re (from 1 to 81), the film thickness increases gradually. The free surface oscillation significantly increases when Re varies from 1 to 35. After the critical point, the free surface tends to be stable. The maximum oscillation occurs at the resonance point ($Re=35$). Therefore, with resonance, the film surface oscillation is the highest. When Re is relatively small ($Re=1$), two minor eddies appear in the corrugation bottom. The scale of the eddy in the left section is larger than the eddy in the right section under all circumstances. As Re increases from 1 to 81, the eddy in the right section of the corrugation bottom gradually decreases at first and finally disappears. The eddy in the left section shows a complex trend. The rotation direction of the two eddies in the bottom is clockwise. However, the vortex at the left bottom will always exist, and the vortex at the right bottom will disappear with the increase in Re . The vortex at the left bottom is similar to the lid-driven cavity flow. The fluid film in the plate region drives the fluid in the left corner and forms the recirculation zone. When the flow rate increases, the lid-driven cavity phenomenon would be enhanced, resulting in the increasing scale of the vortex. The eddy in the right section is primarily caused by the obstruction of the right wall in the flow direction. When the flow rate increases, the effect of this obstruction would gradually decrease and the vortex would gradually decrease until it disappears. The local study of the eddy in the left corner has been performed by simulations and experiments.

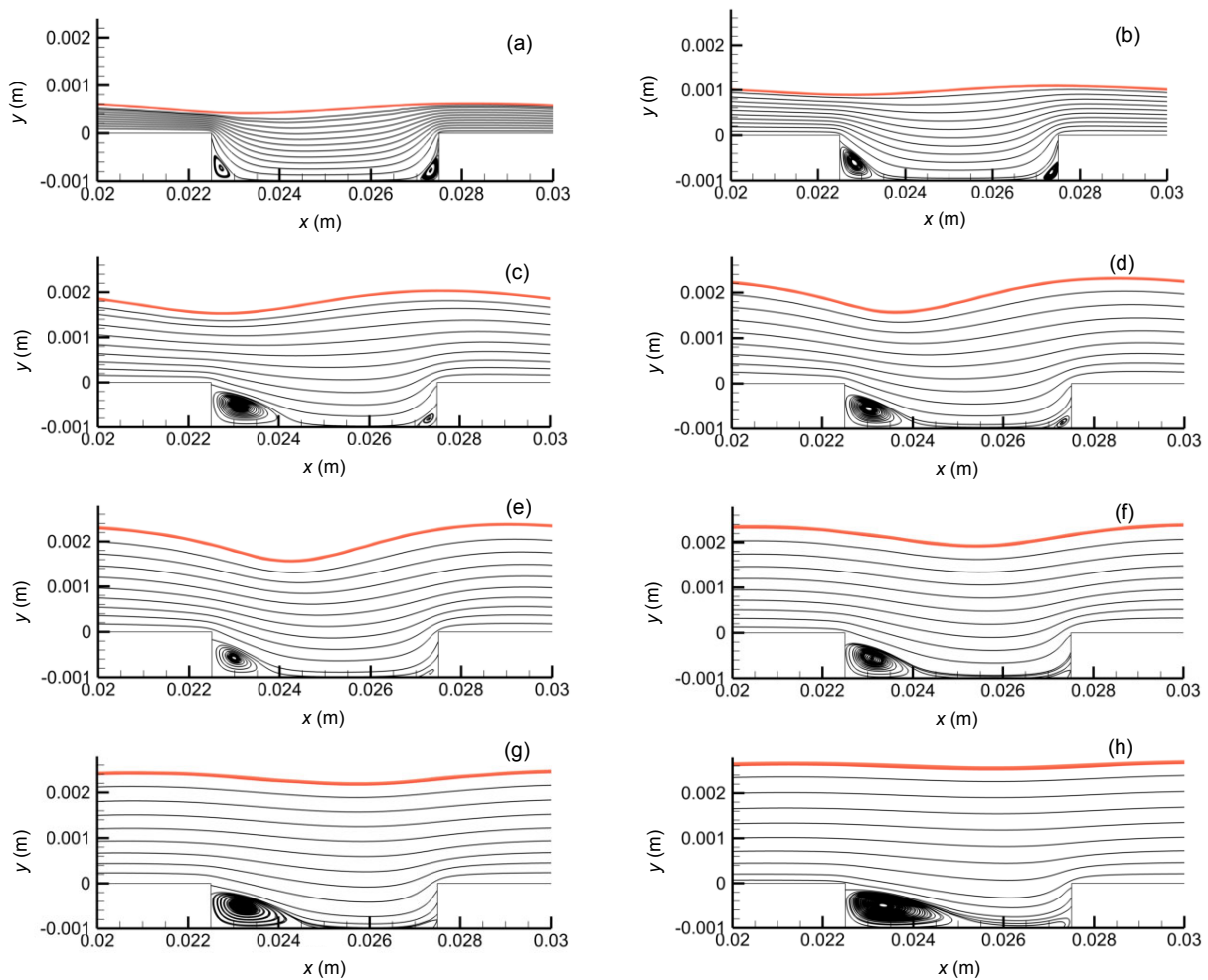


Fig. 4 Flow fields in different Reynolds numbers
 (a) $Re=1$; (b) $Re=5$; (c) $Re=23$; (d) $Re=31$; (e) $Re=35$; (f) $Re=47$; (g) $Re=57$; (h) $Re=81$

3.2 Bottom eddies and resonance section

To study the bottom eddy quantitatively, a dimensionless number E is defined:

$$E=B_a/L_0, \quad (11)$$

where B_a is the eddy length in horizontal direction and L_0 is the length of the rectangular corrugation bottom.

Fig. 5 shows the simulation results of the eddy area in different Re . As Re increases in a low range (from 1 to 23), the eddy size increases accordingly. Subsequently, the eddy size decreases when Re varies from 23 to 35. After the critical point ($Re=35$), the eddy size tends to increase. To verify the relationship between the sizes of the bottom eddies and the resonance phenomenon, we captured pictures of the

bottom eddies in different Re . Because the size of the selected corrugated board is small, a microlens is used for capturing and the view field is limited to a circle. Fig. 6 (p.154) shows the experimental results. The scale and the shape of the eddies in the experiments are similar with those of the simulation results. Generally, the scale of the eddies increases with the increase in Re . The eddies are suppressed within a range of Re . The suppression reaches the largest when Re is 31. The variations in the eddies reveal a similar trend in the simulations and experiments.

Fig. 7 (p.154) shows the change in eddy size based on different Re . The Re interval is 2 in Fig. 7b. Two inflection points occur in Fig. 7b. In the experiment, one inflection point has been captured. When Re varies from 23 to 35 (resonance point), the eddy size shows a noticeable reduction in the experiment

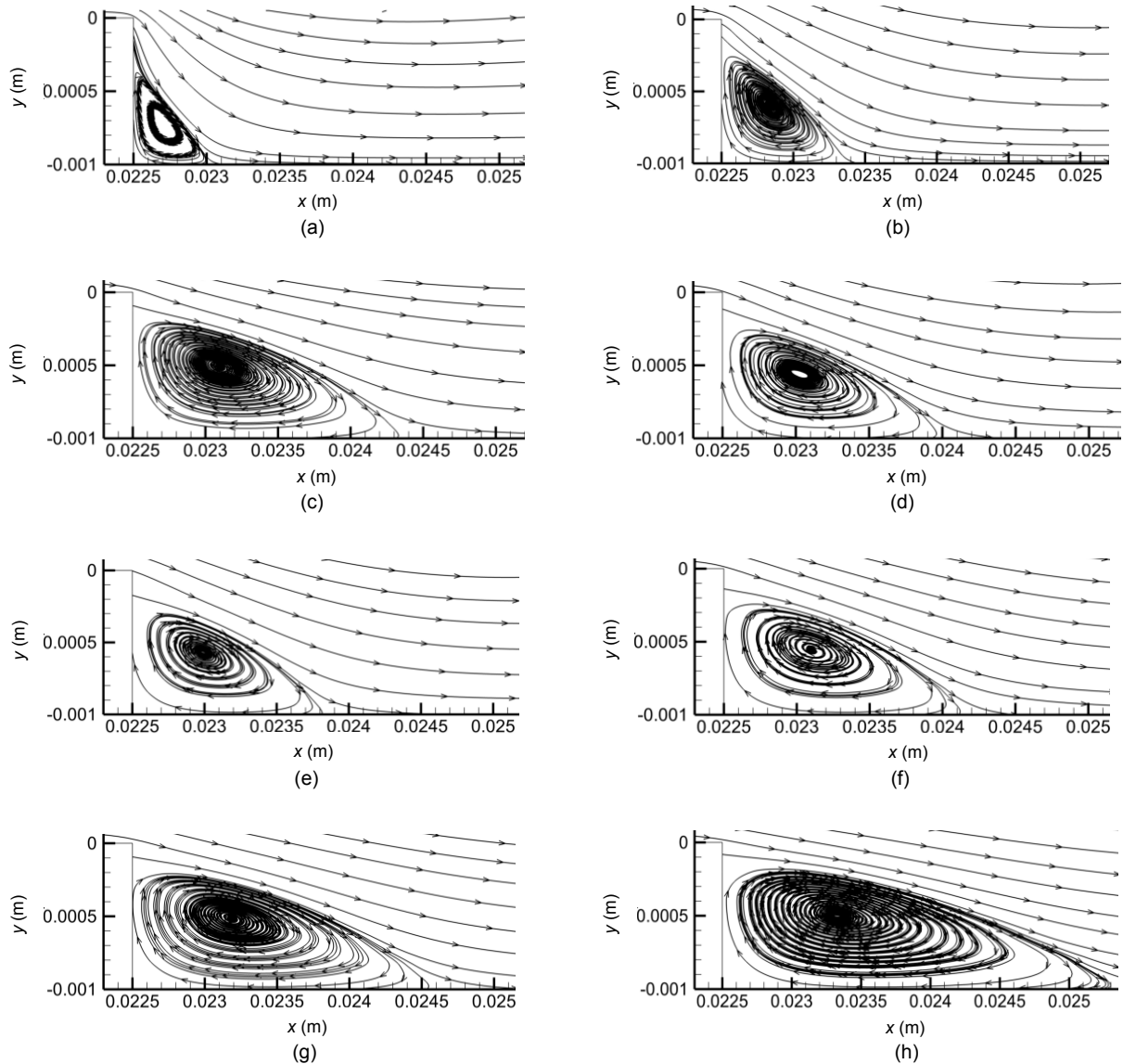


Fig. 5 Eddy areas in different Reynolds numbers

(a) $Re=1$; (b) $Re=5$; (c) $Re=23$; (d) $Re=31$; (e) $Re=35$; (f) $Re=47$; (g) $Re=57$; (h) $Re=81$

and simulation data. This implies that the bottom eddies are suppressed before the resonance phenomenon occurs. The eddy size at the resonance point decreases by 25% relative to the peak ($Re=23$). The experimental data show the same trend. Because the experiment data are not as many as the simulation data, some differences appear between the experimental and simulation results.

Eddy suppression occurs in a certain Re region, and the inhibition effect is enhanced at the resonance point. We suppose that a resonance section exists in which the oscillation of the film surface is enhanced,

and the bottom eddies are suppressed. In Fig. 7b, the eddy sizes of $Re=23$ and $Re=53$ both increase by 25% compared with that at the resonance point. In this operating condition, the region (Re varying from 23 to 53) is defined as the resonance section. The detailed study on the inhibition impact of the resonance section on the bottom eddies is performed in the following section.

3.3 Free surface amplitude

The most widely studied parameter hitherto is the free surface amplitude. For film flow, the increase

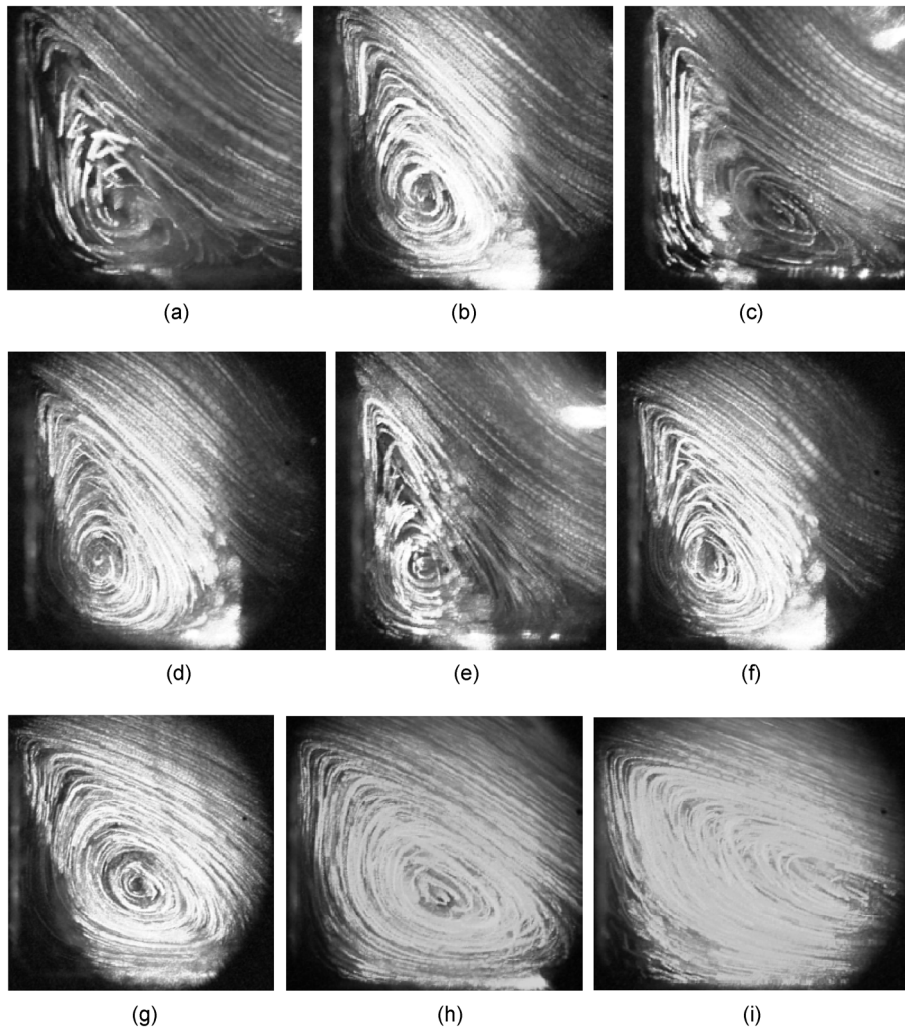


Fig. 6 Eddy areas in different Reynolds numbers (experimental results)
 (a) $Re=1$; (b) $Re=5$; (c) $Re=23$; (d) $Re=28$; (e) $Re=31$; (f) $Re=43$; (g) $Re=47$; (h) $Re=57$; (i) $Re=81$

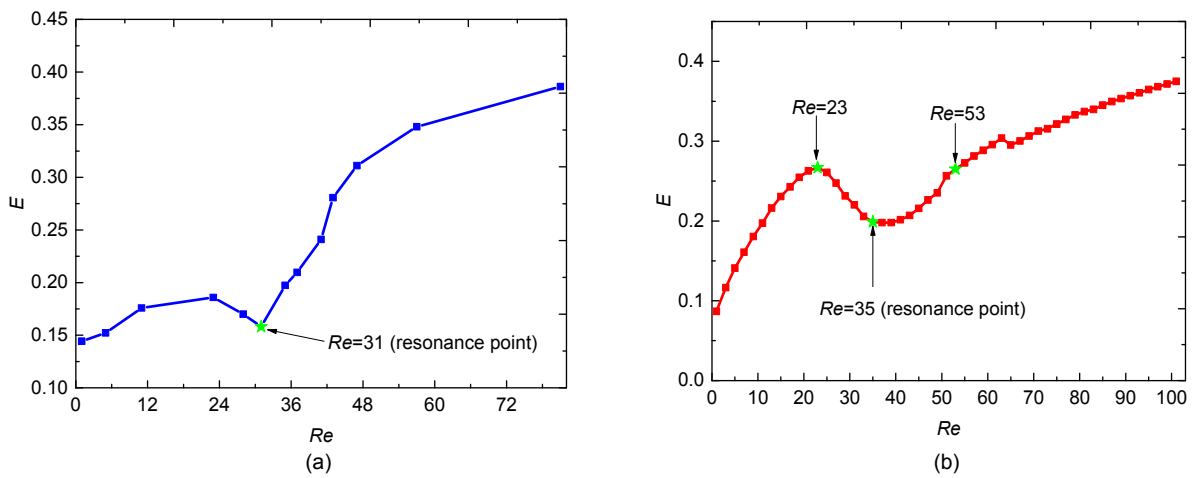


Fig. 7 Transformation law of eddy size with different Reynolds numbers
 (a) Experimental data; (b) Simulation data

in the free surface amplitude causes the film to fluctuate more violently, thus implying that the gas and liquid possess a greater contact area. We define the dimensionless relative amplitude R as

$$R=H/A, \tag{12}$$

where H is the free surface amplitude.

One inflection point appears in the relative amplitude line in Figs. 8a and 8b. In Fig. 8a, the relative amplitude reaches the maximum of 0.58 when Re is 31. In Fig. 8b, when Re is 35, R reaches the maximum value (0.81). With the increase in Re , the relative amplitude increases at first and subsequently decreases, as shown in Fig. 8. In the beginning, the slope of the curve is small. The trend is relatively flat when Re is in the range of 70 to 100. The trends of the amplitude with the increase in Re are similar in the experiments and simulations.

In section 3.2, Re from 23 to 53 are defined as the resonance section. In Fig. 8c, the slope of the curve contains two inflection points. The first inflection point ($Re=23$) corresponds to the lower bound of the resonance section. The second inflection point ($Re=41$) is lower than the upper bound of the resonance section. However, compared to the maximum of the relative amplitude (0.81), the relative amplitude (0.68) decreases by 17% when Re is 41. Compared to the maximum of the relative amplitude, the relative amplitude (0.50) decreases by 38% when Re is 23. Meanwhile, the relative amplitude (0.33) decreases by 59% when Re is 53.

According to the definition, the resonance section enhances the oscillation of the film surface. It is more reasonable to reset the upper bound of the resonance section as $Re=41$. Therefore, Re from 23 to 41 should represent the resonance section.

3.4 Average thickness of the liquid film

The average thickness of a liquid film (h_N) is an indispensable parameter that is defined as

$$h_N = \frac{1}{m} \sum_{i=1}^m |y_{P_i} - y_{W_i}|, \tag{13}$$

where m is the number of compute nodes on the interface, P_i is the i th compute node of the free surface

sorted by the horizontal ordinates, y_{P_i} is the vertical ordinate of P_i , W_i is the point on the wall whose horizontal ordinate is equal to P_i , and y_{W_i} is the vertical ordinate of W_i .

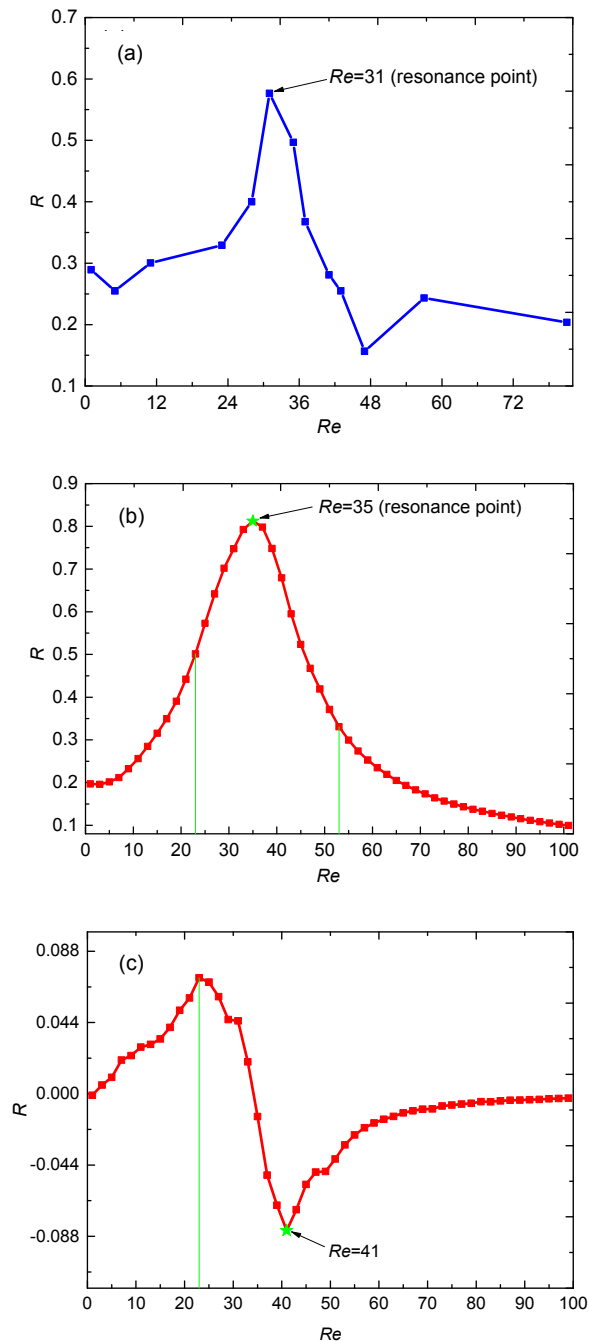


Fig. 8 Transformation law of relative amplitude with different Reynolds numbers

(a) Experimental data; (b) Simulation data; (c) Increment of the simulation data

Fig. 9 shows the transformation law of the average thickness of the liquid film with different Re . The experimental data and simulation data are consistent. In almost all regions, the average thickness of the liquid film increases with the increase in Re . The experimental data of Fig. 9a show that when Re is more than 23, a turn appears in the curve. The average thickness of the liquid film increases slowly until Re is 45. Subsequently, the curve continues to rise with a large slope. The simulation data of Fig. 9b show that the curve becomes gentler in the resonance section. The average thickness of the liquid film at the resonance point is 0.0021 m. The deviation between the simulation data and the experimental data is approximately 28%. Beyond the range of the resonance section, h_N increases with a fixed slope. The results indicate that the resonance section has a suppression effect on the variations in the average liquid film thickness.

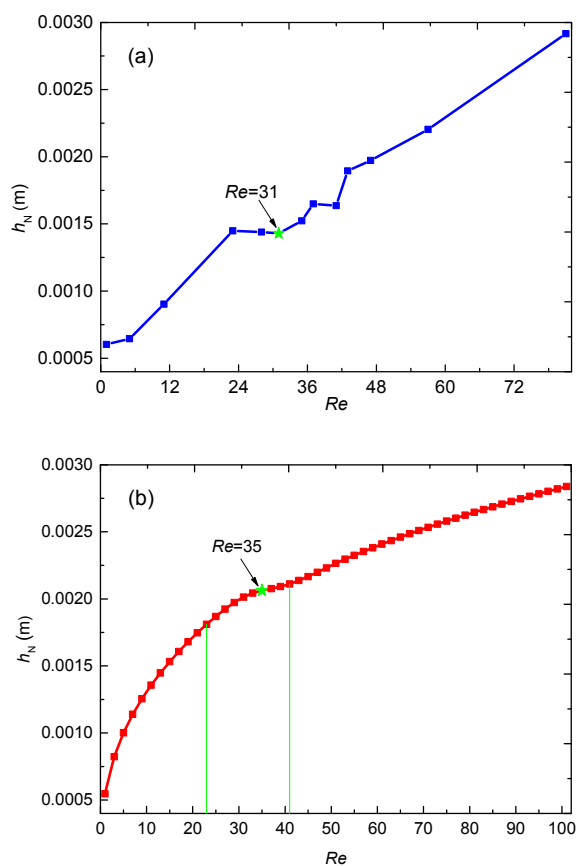


Fig. 9 Transformation law of average thickness of liquid film with different Reynolds numbers

(a) Experimental data; (b) Simulation data

3.5 Velocity distribution in resonance section

3.5.1 Velocity vectors at the resonance point

Fig. 10a shows the experimental results of the velocity vectors distribution when resonance occurs ($Re=31$). The velocities of the upper part of the flow field are larger than those of the bottom part. With the increase in the vertical ordinate, the magnitude of the velocity vectors increases. Fig. 10b shows the simulation results of the velocity vectors when resonance occurs ($Re=35$). The simulation results reveal the similar trend.

In the left corner of the corrugation bottom, the vectors are in a continuous line. A reflux recirculate region occurs in this area. A clear velocity distribution of the bottom eddy cannot be processed from the experimental result of the whole flow field. We perform the PIV treatment on the images captured by the microlens.

Fig. 11 shows the velocity vectors of the bottom eddy. The appearance of the reflux recirculate region is similar to the simulation result. The velocity vectors in the eddy section are much smaller than those of other sections.

3.5.2 Velocity distribution of free surface

The velocity distributions of free surfaces at specific Re are studied in this section. $Re=1$ is the condition implying a low Re . $Re=23$ and $Re=41$ are occurs. $Re=81$ is the condition implying a high Re . We define the flow direction as the x -direction, and the direction vertical to the flow as the y -direction.

Fig. 12 shows the velocity distributions of the free surface in the x -direction (U_x). The range of the horizontal ordinates is from 0.01 m to 0.06 m, which corresponds to five continuous periodic corrugations. With the increase in Re , the U_x of every point on the free surface is increased. The velocity distributions of the free surface at all Re show the characteristic of periodic change. The changes in velocities are relatively small when $Re=1$ and $Re=81$. The curve is almost flat when $Re=81$. The free surface amplitudes are also small in these two conditions. For points in the resonance section ($Re=23, 35, 41$), the changes in U_x are significant. Additionally, the free surface amplitudes are high. U_x is significantly affected by Re . As the surface oscillation of the film flow intensifies,

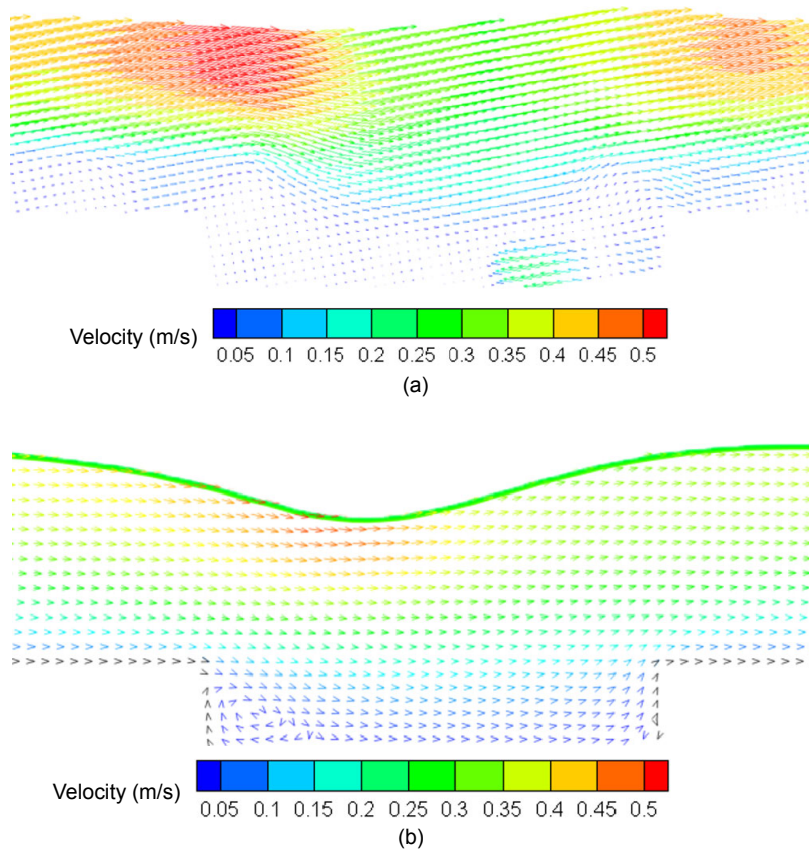


Fig. 10 Velocity vectors at the resonance point
(a) Experimental result; (b) Simulation result

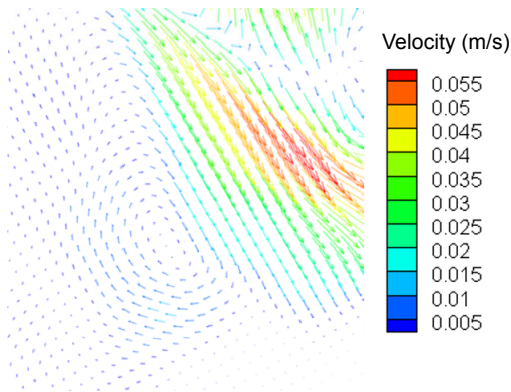


Fig. 11 Velocity vectors of bottom eddy (experimental result)

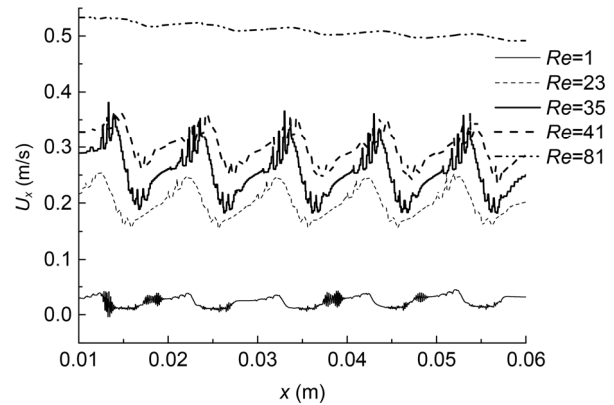


Fig. 12 Velocity distributions of the free surface in x -direction

the differences in U_x between the points on the free surface follow suit.

Fig. 13 shows the velocity distributions of the free surface in the y -direction (U_y) at certain Re . The

higher the normal velocity of the liquid, the greater the transfer between air and liquid. The change in U_y also shows the characteristic of periodicity. The value of U_y is periodically changing between positive and

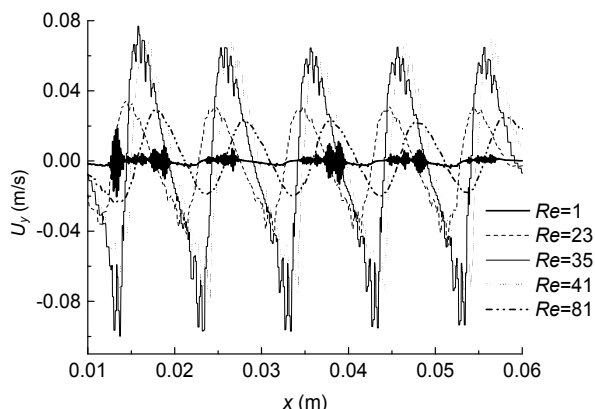


Fig 13 Velocity distributions of the free surface in *y*-direction

negative, and it is significantly less than the value of U_x . When Re is low ($Re=1$) and high ($Re=81$), U_y is relatively small. U_y at the resonance point reaches the maximum. In the resonance section, U_y is enhanced.

The normal velocities of the free surface are affected by resonance. To study the transformation law of velocity with different Re , the intensity of the normal velocity is defined as

$$I_n = \frac{1}{m} \sum_{i=1}^m |U_{ni}|, \quad (14)$$

where m is the number of compute nodes on the free surface, and U_{ni} is the normal velocity of each compute node on the free surface, which is vertical to the flow direction. I_n characterizes the flow situation of the free surface.

In Fig. 14, the transformation law of I_n is similar to that of the free surface amplitude. However, when Re is high, the free surface amplitude tends to be zero, while I_n is still large. The normal velocity intensity (19.79×10^{-3} m/s) at $Re=23$ decreases by 47% compared with the peak (41.59×10^{-3} m/s). I_n (36.20×10^{-3} m/s) at $Re=41$ decreases by 13% compared with the peak. It can be concluded that the resonance section enhances the normal velocity intensity of the free surface.

3.5.3 Velocity distribution on a profile

To study the velocity distribution on a profile (a line for the 2D model), we set 100 sampling points

along the line ($x=0.025$ m) uniformly. The vertical ordinates of these points range from the corrugation bottom to the free surface. Fig. 15 shows the sampling setting.

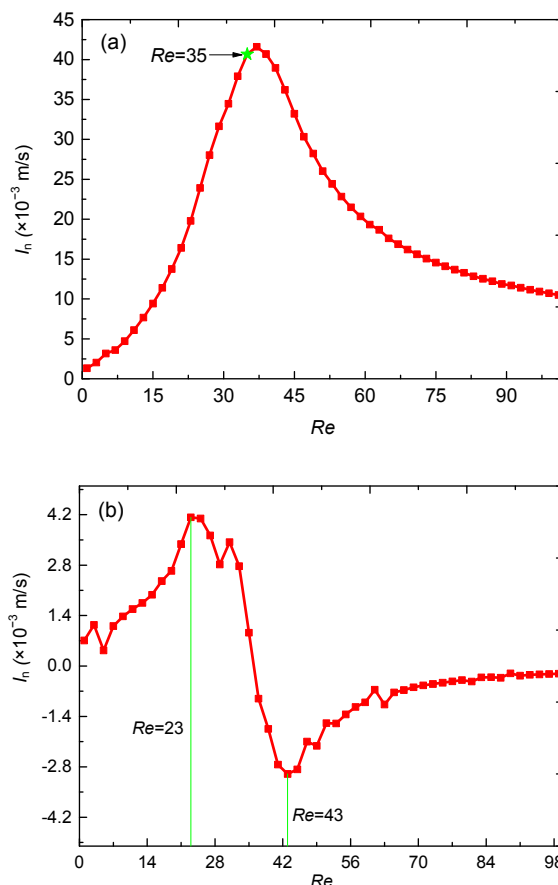


Fig. 14 Transformation law of normal velocity intensity with different Re

(a) Normal velocity intensity of the free surface; (b) Increment in normal velocity intensity

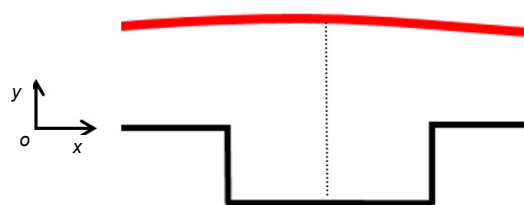


Fig. 15 Sampling setting (100 points)

Fig. 16 shows the velocity distributions at $x=0.025$ m at certain Re . Because of different liquid thicknesses, the curve under different Re exhibits a

distinct height. The curves with different heights illustrate that the liquid thickness is the smallest when Re is 1, and the liquid thickness increases subsequently. After entering the resonance section ($Re=23$), the liquid thickness shows a sluggish growth. When Re is high ($Re=81$), the liquid thickness reaches the maximum value, showing significant growth.

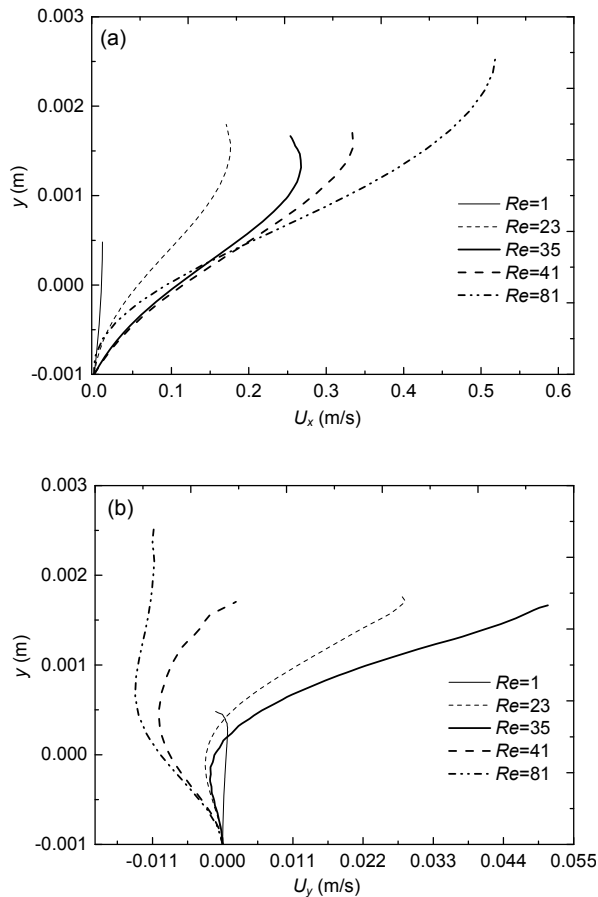


Fig. 16 Velocity distributions ($x=0.025$ m)

(a) Velocity distributions in x -direction; (b) Velocity distributions in y -direction

Regarding the U_x of the profile, the curve demonstrates a parabola similarity distribution from the bottom to top under certain Re . U_x is zero due to the non-slip condition at the bottom, and increases as y becomes larger. Further, U_x tends to be stable and even decreases slightly at the location close to the free surface because of surface tension. As the variation in Re is caused by the change in U_x , U_x increases with Re . We observed that U_x is close to zero when Re is 1.

Further, when Re is high ($Re=81$), U_x at the free surface reaches the maximum value. In addition, the formation of the bottom eddy influences the distribution of U_x . When Re is high ($Re=81$), the U_x of the point at the bottom where the eddy is large is decreased compared with conditions in the resonance section. The eddies are depressed in the resonance section; therefore, U_x at the bottom is relatively large in the resonance section.

As for the U_y of all sampling points at $x=0.025$ m, the curves in Fig. 16b show three types of change tendency. Similar to U_x at the bottom, U_y at the bottom under all Re is zero caused by the non-slip condition. One of the change tendencies is that the U_y of the profile increases at first and subsequently decreases. U_y is positive along most locations, and tends to be negative close to the interface. The situation occurs when Re is small, where the eddy is small as well, which slightly influences the velocity. One is that the U_y of the profile decreases at first and subsequently increases to zero or even to a large positive value. This situation occurs when Re is lower than that at the upper bound of the resonance section ($Re=41$), where the eddy at the bottom can influence the distribution of U_y at the bottom. It is noticeable that U_y at the resonance point ($Re=35$) is greater than that in other conditions, and exhibits the largest rate of change near the interface. The other is that the U_y of the profile decreases at first and subsequently increases. However, the whole U_y distribution is negative. The situation occurs when Re is high, and the eddy size under such Re is sufficiently large to affect the center of the corrugated plate.

4 Conclusions

Film flow resonance could maximize the oscillations of a free surface. The resonance phenomenon was related with a range of Re rather than a specific Re . We proposed the resonance section, in which the oscillation of the film surface was enhanced and the bottom eddies were suppressed. Simulations and experiments were performed to study the film flow resonance. The results demonstrated that:

1. The suppression of eddies occurred in a certain Re region, and it was the most obvious at the

resonance point. The upper and lower bounds of the resonance section corresponded to the two inflection points of the free surface amplitude.

2. The resonance phenomenon exhibited a suppression effect on the increase in the average liquid film thickness. In the resonance section, the average thickness of the liquid film increased more slowly than the other sections and even decreased.

3. The velocities of the reflux recirculate region were much slower than those of other regions. In regions close to the free surface, the normal velocities were larger. As the surface oscillation of the film flow intensified, the velocity difference in the x -direction (flow direction) between the points on the free surface followed suit. The normal velocity intensity of the free surface was enhanced in the resonance section. In the corrugation bottom region, the velocities in the x -direction were increased by resonance.

In the resonance section, free surface oscillation was enhanced, which was beneficial to mass transfer. This study could subsequently support mass transfer investigations. For the selections of operating conditions in industrial film flow applications, this study could provide the theoretical basis.

References

- Argyriadi K, Vlachogiannis M, Bontozoglou V, 2006. Experimental study of inclined film flow along periodic corrugations: the effect of wall steepness. *Physics of Fluids*, 18(1):012102.
<https://doi.org/10.1063/1.2163810>
- Bontozoglou V, 2000. Laminar film flow along a periodic wall. *Computer Modeling in Engineering & Sciences*, 1(2): 133-142.
<https://doi.org/10.3970/cmcs.2000.001.293>
- Bontozoglou V, Papapolymerou G, 1997. Laminar film flow down a wavy incline. *International Journal of Multiphase Flow*, 23(1):69-79.
[https://doi.org/10.1016/s0301-9322\(96\)00053-5](https://doi.org/10.1016/s0301-9322(96)00053-5)
- Brackbill JU, Kothe DB, Zemach C, 1992. A continuum method for modeling surface tension. *Journal of Computational Physics*, 100(2):335-354.
[https://doi.org/10.1016/0021-9991\(92\)90240-y](https://doi.org/10.1016/0021-9991(92)90240-y)
- Conn JJA, Duffy BR, Pritchard D, et al., 2017. Simple waves and shocks in a thin film of a perfectly soluble anti-surfactant solution. *Journal of Engineering Mathematics*, 107(1):167-178.
<https://doi.org/10.1007/s10665-017-9924-8>
- Gu F, 2004. CFD Simulations of the Local-flow and Mass-transfer in the Structured Packing. PhD Thesis, Tianjin University, Tianjin, China (in Chinese).
- Heining C, Bontozoglou V, Aksel N, et al., 2009. Nonlinear resonance in viscous films on inclined wavy planes. *International Journal of Multiphase Flow*, 35(1):78-90.
<https://doi.org/10.1016/j.ijmultiphaseflow.2008.07.005>
- Hirt CW, Nichols BD, 1981. Volume of fluid (VOF) method for the dynamics of free boundaries. *Journal of Computational Physics*, 39(1):201-225.
[https://doi.org/10.1016/0021-9991\(81\)90145-5](https://doi.org/10.1016/0021-9991(81)90145-5)
- Ho WK, Tay A, Lee LL, et al., 2004. On control of resist film uniformity in the microlithography process. *Control Engineering Practice*, 12(7):881-892.
<https://doi.org/10.1016/j.conengprac.2003.12.001>
- Li J, 2015. Numerical Simulation and Experimental Research on Film Flow of Corrugated Packing Surface. MS Thesis, Zhejiang University, Hangzhou, China (in Chinese).
- Li J, Guo YQ, Tong ZY, et al., 2015. Comparative study on the characteristics of film flow with different corrugation plates. *Microgravity Science and Technology*, 27(3):171-179.
<https://doi.org/10.1007/s12217-015-9429-x>
- Li PP, Chen ZQ, Shi J, 2018. Numerical study on the effects of gravity and surface tension on condensation process in square minichannel. *Microgravity Science and Technology*, 30(1-2):19-24.
<https://doi.org/10.1007/s12217-017-9570-9>
- Li QS, Wang T, Dai CN, et al., 2016. Hydrodynamics of novel structured packings: an experimental and multi-scale CFD study. *Chemical Engineering Science*, 143:23-35.
<https://doi.org/10.1016/j.ces.2015.12.014>
- Malamataris NT, Bontozoglou V, 1999. Computer aided analysis of viscous film flow along an inclined wavy wall. *Journal of Computational Physics*, 154(2):372-392.
<https://doi.org/10.1006/jcph.1999.6319>
- Nabil M, Rattner AS, 2017. A computational study on the effects of surface tension and Prandtl number on laminar-wavy falling-film condensation. *Journal of Heat Transfer*, 139(12):121501.
<https://doi.org/10.1115/1.4037062>
- Nieves-Remacha MJ, Yang L, Jensen KF, 2015. OpenFOAM computational fluid dynamic simulations of two-phase flow and mass transfer in an advanced-flow reactor. *Industrial & Engineering Chemistry Research*, 54(26): 6649-6659.
<https://doi.org/10.1021/acs.iecr.5b00480>
- Pak M, 2011. Research on the Dynamics of Liquid Film Flowing Down a Corrugated Wall. PhD Thesis, Shanghai University, Shanghai, China (in Chinese).
- Paschke S, 2011. Experimentelle Analyse Ein- und Zweiphasiger Filmstroemungen auf Glatten und Strukturierten Oberflaechen. PhD Thesis, TU Berlin, Berlin, Germany (in German).
- Pavlenko AP, Volodin OA, Surtaev AA, 2017. Hydrodynamics in falling liquid films on surfaces with complex geometry. *Applied Thermal Engineering*, 114:1265-1274.
<https://doi.org/10.1016/j.applthermaleng.2016.10.013>

- Schörner M, Reck D, Aksel N, 2016. Stability phenomena far beyond the Nusselt flow—revealed by experimental asymptotics. *Physics of Fluids*, 28(2):022102. <https://doi.org/10.1063/1.4941000>
- Tong ZY, Marek A, Hong WR, et al., 2013. Experimental and numerical investigation on gravity-driven film flow over triangular corrugations. *Industrial & Engineering Chemistry Research*, 52(45):15946-15958. <https://doi.org/10.1021/ie303038c>
- Trifonov Y, 2014. Stability of a film flowing down an inclined corrugated plate: the direct Navier-Stokes computations and Floquet theory. *Physics of Fluids*, 26(11):114101. <https://doi.org/10.1063/1.4900857>
- Trifonov YY, 2016. Viscous liquid film flow down an inclined corrugated surface. Calculation of the flow stability to arbitrary perturbations using an integral method. *Journal of Applied Mechanics and Technical Physics*, 57(2):195-201. <https://doi.org/10.1134/S0021894416020012>
- Vlachogiannis M, Bontozoglou V, 2002. Experiments on laminar film flow along a periodic wall. *Journal of Fluid Mechanics*, 457:133-156. <https://doi.org/10.1017/s0022112001007637>
- Wang YP, Zhou LQ, Kang X, et al., 2017. Experimental and numerical optimization of direct-contact liquid film cooling in high concentration photovoltaic system. *Energy Conversion and Management*, 154:603-614. <https://doi.org/10.1016/j.enconman.2017.11.014>
- Wierschem A, Bontozoglou V, Heining C, et al., 2008. Linear resonance in viscous films on inclined wavy planes. *International Journal of Multiphase Flow*, 34(6):580-589. <https://doi.org/10.1016/j.ijmultiphaseflow.2007.12.001>
- Wierschem A, Pollak T, Heining C, et al., 2010. Suppression of eddies in films over topography. *Physics of Fluids*, 22(11):113603. <https://doi.org/10.1063/1.3504374>
- Wu SQ, Cai L, Yuan MC, et al., 2016. Influence of counter-current airflow on the film flow characteristics. *Chemical Engineering*, 44(12):45-49 (in Chinese). <https://doi.org/10.3969/j.issn.1005-9954.2016.12.010>
- Xu YY, 2010. Computational Fluid Dynamics Modeling and Validation to Portray the Liquid Flow Behavior for Multiphase Flow. PhD Thesis, Shanghai Jiao Tong University, Shanghai, China (in Chinese).

Appendix A: Gridding independence

The inlet liquid film thickness could be considered as the characteristic length, which is divided into different segments in a range of 4 to 45. Fig. A1 shows the flow fields in 10, 17, 24, 31, 38, and 45 segments, where N_{grid} is the number of the grids at the liquid inlet. The meshing grid in the flow direction is

of the same size in the thickness direction to ensure the accuracy of calculation.

$$E_{\text{pro}} = \frac{|p_i - p_{45}|}{|p_{45}|} \times 100\%, \quad i = 4, 5, \dots, 44, \quad (\text{A1})$$

where E_{pro} is the relative error, and p_i is the vortex scale of the model with i elements in the liquid film.

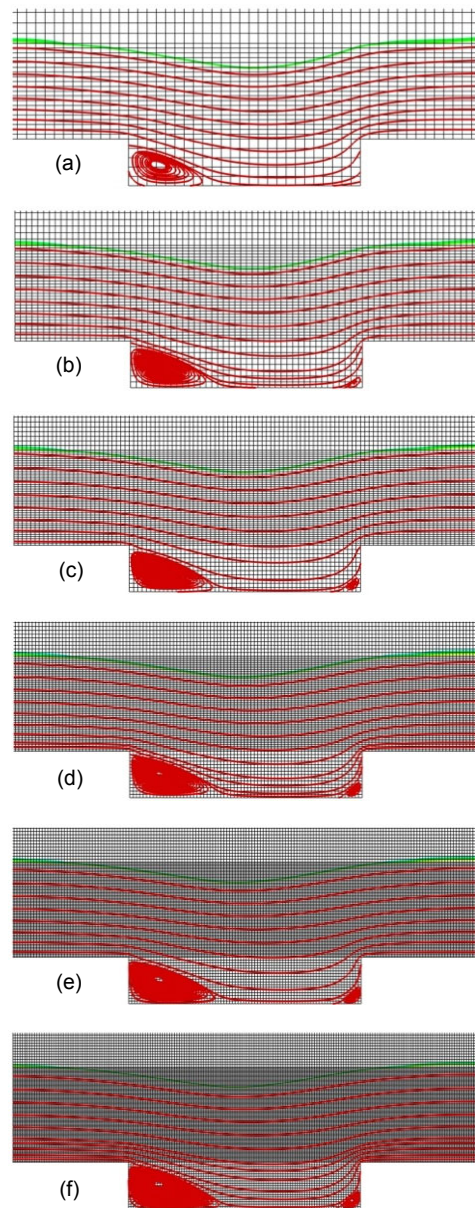


Fig. A1 Flow fields in different grids
(a) $N_{\text{grid}}=10$; (b) $N_{\text{grid}}=17$; (c) $N_{\text{grid}}=24$; (d) $N_{\text{grid}}=31$; (e) $N_{\text{grid}}=38$; (f) $N_{\text{grid}}=45$

The scales of the vortices of the model with elements in the liquid film from 4 to 44 are compared with the 45-element model. Fig. A2 shows that the error is less than 1.2% when the film thickness direction is 6 segments. As the number of grids increases, the error is decreased. When the grid number is more than 15, changes in the error become small. Therefore,

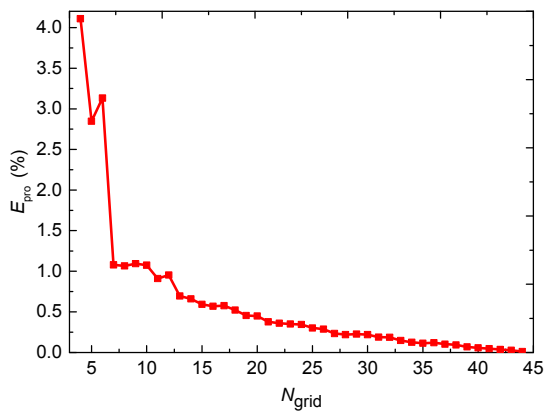


Fig. A2 Grid independence

the model with 15 meshes in the film thickness direction would be the standard.

中文概要

题目: 波纹板薄膜流体共振现象的数值及实验研究

目的: 探究薄膜流体共振现象的内在机理。

创新点: 1. 提出薄膜流体共振区的概念。2. 提出共振现象与雷诺数的范围有关、而不是与某一特定的雷诺数有关的观点。

方法: 1. 使用有限体积法对薄膜流进行数值模拟计算。2. 为了验证模拟的准确性, 运用粒子图像测速法进行实验测量。

结论: 1. 薄膜流体共振可以使自由表面的振荡最大化。2. 共振现象与雷诺数的范围有关, 而不是与特定的雷诺数有关。3. 在共振区域中, 薄膜表面的振动增强, 底部涡流被抑制, 并且这些都有利于传热传质效率的提高。

关键词: 薄膜流体; 共振区; OpenFOAM; 粒子图像测速法; 波纹板